Research Square

Preprints are preliminary reports that have not undergone peer review.
They should not be considered conclusive, used to inform clinical practice,
or referenced by the media as validated information.

Vibration-Based Mass Sensing with Functionally Graded Graphene-Reinforced Piezoelectric Microcantilevers in Air and Liquid

Reza Ghaderi

reza.ghaderi@iau.ac.ir

Islamic Azad University of Shahrekord

Research Article

Keywords: Microcantilever mass sensor, Graphene nanoplatelet-reinforced composite, Functionally graded materials, Piezoelectric actuation, Liquid-phase sensing, Resonance frequency shift, Sobol' sensitivity analysis

Posted Date: November 13th, 2026

DOI: https://doi.org/10.21203/rs.3.rs-11552084/v1

License: This work is licensed under a Creative Commons Attribution 4.0 International License.
Read Full License

Additional Declarations: No competing interests reported.

Vibration-Based Mass Sensing with Functionally Graded Graphene-Reinforced Piezoelectric Microcantilevers in Air and Liquid

Abstract

Resonant microcantilevers are widely used for mass sensing, yet the effects of material architecture and operating medium remain unclear. This study develops an analytical model of a multilayer graphene nanoplatelet-reinforced composite (GPLRC) piezoelectric microcantilever with a narrowed tip. The formulation combines Euler–Bernoulli beam theory, a modified Halpin–Tsai model, a piecewise modal solution incorporating adsorbed mass, and a string-of-spheres hydrodynamic model. Uniform (U) and functionally graded (X, O, A) platelet distributions are investigated in epoxy, polyamide 6 (PA6), and polypropylene (PP) matrices. Validation against published measurements yields deviations of 2.2% in air and 0.3–2.3% in liquids. Adsorption of a 20ng particle decreases resonance frequency. The relative shift in water is nearly ten times smaller than in air and decreases with increasing glycerol concentration. O-GPLRC produces the largest frequency shift in both media. PP performs best in air, whereas PA6 performs best in liquids. Amplitude-based responses rank configurations differently from frequency-based metrics. Higher platelet content reduces relative frequency shifts through stiffening. Sobol' analysis identifies platelet width and thickness as dominant parameters, contributing 52–54% and 41–44% of variance, respectively, while length contributes less than 5%. These findings support optimizing material architecture, matrix, medium, and readout metric.

Keywords: Microcantilever mass sensor; Graphene nanoplatelet-reinforced composite; Functionally graded materials; Piezoelectric actuation; Liquid-phase sensing; Resonance frequency shift; Sobol' sensitivity analysis.

1.Introduction

Resonant microcantilevers convert adsorbed mass into a frequency shift, and their dynamic response also reflects the surrounding fluid, because the hydrodynamic load has both an inertial and a dissipative component [1]. Sensitivity depends on how the mass is distributed along the beam and on which flexural mode is used [2]. Recent work on small-scale mass sensors has addressed size effects [3], smart functionally graded microbeams used as micro-mass sensors [4], and frequency shifts caused by several eccentric masses [5]. Shifts in damping are of the same order as shifts in frequency, so amplitude- and damping-based outputs can complement frequency tracking [6]. A sensor design must therefore consider not only the mass to be detected but also the mode, the position of the mass, and the quantity that is read out.

Piezoelectric transduction lets one structure be both driven and read electrically. Multisized piezoelectric cantilever arrays have separated mass loading from surface stress, with femtogram-level mass sensitivity [7]. A self-sensing piezoelectric cantilever, modeled and tested experimentally, gave adsorbed-mass readings that agreed with optical detection to 99.63% [8]. In a recent piezoelectrically actuated diamond microcantilever, the eigenfrequency was matched to the AlN actuator, and the frequency shift for a Gaussian-distributed mass fell from 600 Hz to 100 Hz as the mass center moved from the tip to the piezoelectric border [9]. Resonance-frequency calibration against known added mass has also been used to estimate adsorbed gas mass on piezoelectrically driven microcantilevers [10]. These studies show that piezoelectric cantilevers can serve as compact mass sensors, and they motivate attention to the structural layer, which sets stiffness and mass.

Operation in liquid adds hydrodynamic inertia and dissipation. Sader's framework for cantilevers in viscous fluids [11] was extended to arbitrary mode order [12]. Reviews note that hydrodynamic forces on flexural

resonators allow density and viscosity to be sensed simultaneously [13]. Water–glycerol mixtures have long been used to probe how liquid density and viscosity affect resonance of piezoelectric cantilevers [14]. Recent piezoelectric resonators have decoupled density and viscosity using two-dimensional flexural modes [15], examined how quality factor depends on viscosity and vibrational mode [16], and measured viscosity directly with a tip-coupled two-cantilever system [17]. A laterally vibrating AlN resonator gave a quality factor that depends linearly on viscosity, which removes the need for density calibration [18]. Perforating the free end of a cantilever has been shown to suppress squeeze-film damping in viscous liquids [19]. These results show that fluid loading depends on both medium and mode, and must be built into the model. Liquid-phase operation therefore cannot be treated as a simple extension of operation in air, and differences in fluid density and viscosity can change the balance between added inertia and damping.

Graphene nanoplatelet-reinforced polymer composites (GPLRCs) allow the stiffness and mass of the structural layer to be tailored. At only 0.1 wt%, graphene platelets raised the tensile strength of epoxy by about 40%, against about 14% for multi-walled carbon nanotubes [20]. Thermoplastic matrices offer other stiffness-to-density combinations. In PA6, 5.25 wt% of graphene nanoplatelets raised Young's modulus by 22% [21], and the modulus rose from 2871 to 3775 MPa as the platelet content grew from 0 to 3% [22]. In PP, small platelets gave a modulus improvement of about 59% [23], whereas larger platelets lowered the tensile modulus [24], and loading with GNPs improved the tensile properties of recycled PP [25]. The choice of matrix and platelet geometry therefore changes the baseline dynamics of the sensor. These data come from mechanical tests of bulk specimens, so they indicate trends in stiffness rather than sensor performance, which has to be evaluated separately. Because the matrix sets the stiffness-to-mass ratio, a matrix that yields a higher natural frequency does not necessarily yield a larger frequency change after adsorption, and rankings by frequency and by amplitude may differ.

Functionally graded GPLRCs (FG-GPLRCs) vary the platelet content through the thickness. The U-, X-, O-, and A-type patterns are defined through layer-wise volume fractions [26]. In cylindrical panels, FG-X gave the highest and FG-O the lowest natural frequencies [27]. Distribution pattern also governs the vibration of beams on elastic foundations in magnetic fields [28], and multilayer FG-GPLRC microplates have been analyzed with the Halpin–Tsai model under thermal loading on a viscoelastic medium [29]. Free vibration and buckling of FG plates with GPL reinforcement were studied in [30]. The best pattern depends on structure and criterion, so it cannot be assumed to be optimal for mass sensing. Because the reinforcement distribution changes bending stiffness and modal mass in different ways, a frequency ranking alone does not reveal the effect on the response to an added mass.

Graphene reinforcement has also been combined with piezoelectricity. Linear and nonlinear vibrations of GPL-reinforced functionally graded piezoelectric microplates were studied with nonlocal theory [31], smart microplates with a GPL-reinforced FGM core and piezoelectric coatings were analyzed on an elastic foundation[32], and electro-thermal vibration of GPL-reinforced piezoelectric microplates was addressed in [33]. Piezoelectric patches on FG graphene-reinforced cantilever plates were used to attenuate vibration amplitude for four graphene distributions [34]. Fluid interaction has been treated for FG-GPLRC beams partially in contact with fluid [35] and for plates in contact with fluids on both sides, including the effect of fluid depth on frequencies and mode shapes [36]. These studies concentrate on free vibration, control, and natural frequencies. This distinction matters because a structure optimized for vibration control or for a high natural frequency is not necessarily the most effective configuration for detecting an adsorbed particle. To the authors' knowledge, nanoparticle-induced changes in the frequency and amplitude of a piezoelectric GPLRC microcantilever have not been compared across reinforcement distributions, matrices, modes, and fluid media in one framework, nor has the influence of GPL geometry on these responses been quantified.

Quantifying that influence calls for global sensitivity analysis. One-at-a-time variation, by contrast, shows individual trends but cannot rank inputs across the whole design space. For GPLRC microcantilevers this

matters because GPL length, width, and thickness affect the effective properties through different geometric contributions. Variance-based indices computed by Monte Carlo methods [37] and total-effect estimators [38] capture both individual and interaction effects, and a recent application analyzed the moduli of carbon fiber reinforced polymer with twelve input properties [39].

This study therefore develops an analytical model of a multilayer GPLRC piezoelectric microcantilever for resonant mass sensing. The main contributions are as follows. First, a unified formulation is presented for the piezoelectric multilayer microcantilever with nanoparticle adsorption, in which U-, X-, O-, and A-type GPL distributions are treated within perfectly bonded laminas. Second, the frequency and amplitude responses of epoxy-, PA6-, and PP-based microcantilevers are compared across vibration modes, which shows how matrix selection interacts with reinforcement distribution in governing the sensing response. Third, the sensing response is assessed in air, water, and water–glycerol mixtures, so that the dependence on the surrounding medium can be examined under different fluid conditions. Finally, a Sobol-based global sensitivity analysis quantifies the influence of GPL length, width, and thickness over the prescribed design ranges. Together, these elements link material design, reinforcement architecture, and operating environment within a single analytical framework, so that design trade-offs can be assessed directly through the predicted frequency and amplitude responses.

2. Material Modeling of Multilayer GPLRC MC

The present study investigates the free-vibration characteristics of a multilayer graphene platelet-reinforced composite (GPLRC) microcantilever (MC) integrated with an active piezoelectric driving layer. The structural component of the MC consists of multiple GPLRC laminas with identical thicknesses that are perfectly bonded to ensure complete strain compatibility between adjacent layers. Each lamina is composed of an isotropic polymer matrix reinforced with graphene platelets (GPLs), which are assumed to be randomly oriented and uniformly dispersed within the matrix plane.

To tailor the mechanical characteristics of the MC, four GPL distribution patterns are considered: a uniform distribution (U-GPLRC) and three functionally graded distributions, namely A-GPLRC, X-GPLRC, and O-GPLRC, as illustrated in Figure 1. The shaded regions in the figure represent the layers with higher GPL concentrations. Since the effective mechanical properties of the composite are strongly affected by the spatial distribution of the nanofillers, these grading patterns provide an effective means of controlling the stiffness distribution through the laminate thickness and, consequently, modifying the dynamic characteristics of the MC.

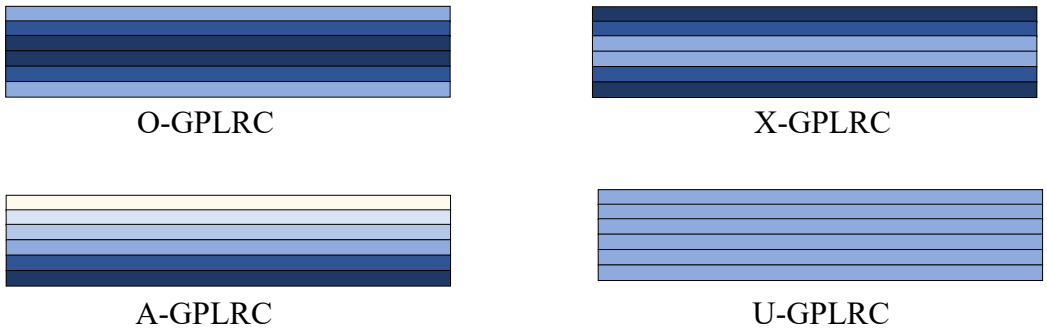


Figure 1. Different GPL distribution patterns in the multilayer GPLRC MC.

For the formulation of the multilayer model, the GPLRC laminate is assumed to consist of an even number of layers. The GPL volume fraction in the nth layer is defined according to the selected distribution pattern shown in Figure 1 and is expressed as follows[40]:

A-GPLRC: $V_{GPL}^{n} = V_{GPL}^{T}|2i-1|/n_L$ (1)

O-GPLRC: $V_{GPL}^{n} = 2V_{GPL}^{T}(1 - |2n - n_L - 1|/n_L)$ (2)

X-GPLRC: $V_{GPL}^{n} = 2V_{GPL}^{T}|2n - n_L - 1|/n_L$ (3)

U-GPLRC: $V_{GPL}^{n} = V_{GPL}^{T}$ (4)

where V_{GPL}^{n} denotes the GPL volume fraction of the ith layer and n_L represents the total number of layers. The overall GPL volume fraction of the laminate is determined from

$$V_{GPL}^{T} = \frac{W_{GPL}}{W_{GPL} + (\rho_{GPL}/\rho_m)(1 - W_{GPL})} \tag{5}$$

where ρ_{GPL} and ρ_m represent the densities of the graphene platelets and polymer matrix, respectively, and WGPL denotes the overall GPL weight fraction of the composite. Although the total GPL content is maintained constant, its distribution across the laminate thickness varies according to the selected grading pattern.

The effective Young's modulus of each GPLRC layer is evaluated using the modified Halpin–Tsai micromechanical model, which accounts for the geometric characteristics and size effects of graphene nanoplatelets [40]. Accordingly, the equivalent Young's modulus of the nth layer is expressed as:

$$E_i = \frac{E_m}{8}\left(3\frac{1 + \gamma_1\zeta_1 V_{GPL}^{i}}{1 - \zeta_1 V_{GPL}^{i}} + 5\frac{1 + \gamma_2\zeta_2 V_{GPL}^{i}}{1 - \zeta_2 V_{GPL}^{i}}\right) \tag{6}$$

where the parameters ζ_1 and ζ_2 are given by

$$\zeta_1 = \frac{E_{GPL}/E_m - 1}{E_{GPL}/E_m + \gamma_1};\ \zeta_2 = \frac{E_{GPL}/E_m - 1}{E_{GPL}/E_m + \gamma_2} \tag{7}$$

In these equations, E_{GPL} and E_P denote the Young's moduli of the graphene platelets and polymer matrix, respectively. The geometric parameters of the GPLs are defined as

$$\gamma_1 = \frac{2L_{GPL}}{h_{GPL}};\ \gamma_2 = \frac{2b_{GPL}}{h_{GPL}} \tag{8}$$

where L_{GPL}, b_{GPL}, and h_{GPL} are the length, width, and thickness of the graphene platelets, respectively. The effective Poisson's ratio of each GPLRC layer is calculated using the classical rule of mixtures:

$$\upsilon = \upsilon_m V_m + \upsilon_{GPL} V_{GPL} \tag{9}$$

where υ_{GPL} and υ_m denote the Poisson's ratios of the graphene platelets and matrix, respectively. Thus, the mechanical properties of each GPLRC layer are determined according to its local GPL content, while the overall GPL content of the laminate remains constant for all considered distribution patterns. This formulation enables the effects of different through-thickness GPL distributions on the dynamic response of the piezoelectric MC to be investigated within a unified multilayer framework.

3. Dynamic Modeling of the Piezoelectric GPLRC MC as a Mass Sensor

The considered microcantilever (MC) has a non-uniform configuration and incorporates an active piezoelectric layer to provide electromechanical excitation. The structural component consists of a multilayer GPLRC laminate, while the piezoelectric layer is positioned between the upper and lower electrodes. The piezoelectric layer induces transverse vibration of the MC through electromechanical coupling when an alternating electrical voltage is applied across the electrodes. The MC is clamped at one end and has a sharp, narrowed section near its free end, forming a geometry suitable for mass sensing.

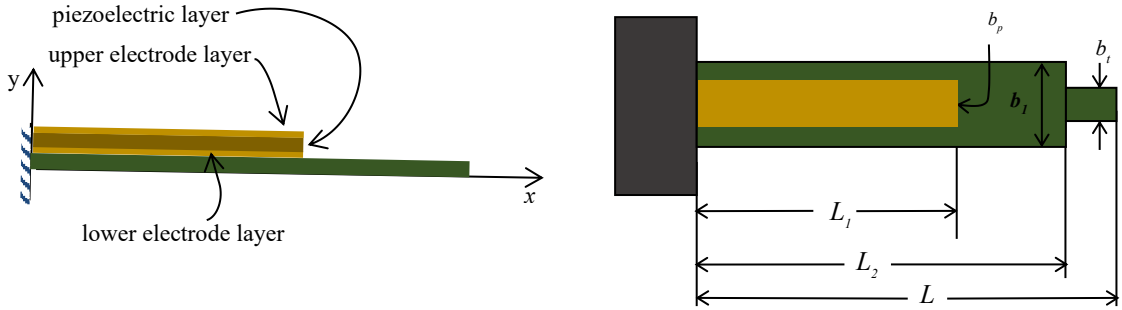


Figure 2. Schematic configuration of the piezoelectric GPLRC MC

The governing equation of motion is derived using Hamilton's principle in conjunction with the Euler–Bernoulli beam theory. Under the assumptions of small transverse deformation and linear elastic behavior, the kinetic energy of the MC can be expressed as

$$T_{MC} = \frac{1}{2}\int_0^L m_0(x)\dot{v}^2(x,t)dx \tag{10}$$

where $v(x,t)$ denotes the transverse displacement of the MC at position (x) and time (t). The equivalent mass per unit length, $m_0(x)$, is given by

$$m_0(x) = \sum_{j=1}^{n_L+3} \rho_j b_j h_j \left(H_0 - H_{L_1}\right) + \sum_{j=1}^{n_L} \rho_j b_j h_j \left(H_{L_1} - H_{L_2}\right) + \rho_1 b_t h_1 \left(H_{L_2} - H_L\right) \tag{11}$$

where ρ, b, and h denote the density, width, and thickness of each layer, respectively. The parameter b_t represents the tip width of the MC, while $H(x)$ is the Heaviside step function, defined such that $H_L=H(x-L)$.

The presence of an adsorbed nanoparticle at the free end introduces an additional concentrated inertial term. The nanoparticle is assumed to be perfectly attached to the MC surface and to move synchronously with the free end of the beam. Accordingly, its kinetic energy is given by:

$$T_P = \frac{1}{2} m_P \dot{v}^2(L,t) \tag{12}$$

where m_p denotes the mass of the adsorbed nanoparticle and $v(L,t)$ represents the transverse displacement at the free end of the MC. Therefore, the total kinetic energy of the system is obtained by combining the distributed inertia of the MC with the concentrated inertia associated with the attached nanoparticle. Therefore, the total kinetic energy of the sensing system is obtained by combining the kinetic energies of the MC and the attached nanoparticle as:

$$T = T_{MC} + T_P \tag{13}$$

or equivalently,

$$T = \frac{1}{2}\int_0^L m_0(x)\dot{v}^2(x,t)dx + \frac{1}{2} m_P \dot{v}^2(L,t) \tag{14}$$

The total potential energy is formulated based on the Euler–Bernoulli beam theory. In this formulation, the beam is assumed to undergo small deflection, while transverse normal and shear strains are neglected. Thus, $\varepsilon_{yy} = \varepsilon_{xy}=0$, and the Poisson effect associated with the bending deformation is neglected. The longitudinal strain is consequently expressed in terms of the distance from the neutral axis of the multilayer cross-section.

For the piezoelectric layer, the application of an alternating voltage across the electrodes generates an electric field and consequently induces electromechanical stress within the piezoelectric material. The constitutive relation of the piezoelectric layer is $\sigma_p = E_p\varepsilon_p - E_p d_{31}P(t)$, therefore introduced by considering its elastic modulus (E_p), the longitudinal strain (ε_p), the piezoelectric coefficient d_{31}, and the applied electrical excitation $P(t)$.

By substituting the corresponding stress–strain relations into the potential-energy expression and integrating over the cross-sectional area, the total potential energy of the piezoelectric GPLRC MC is obtained as

$$U = \frac{1}{2}\int_0^{L_1}\int_A\left(\sigma_{11}^b S_{11}^b + \sigma_{11}^{e_L} S_{11}^{e_L} + \sigma_{11}^{eu} S_{11}^{eu}\right)dAdx + \frac{1}{2}\int_0^{L_1}\int_A \sigma_{11}^p S_{11}^p dAdx + \frac{1}{2}\int_{L_1}^{L}\int_A \sigma_{11}^b S_{11}^b dAdx \tag{15}$$

The resulting stress and strain distributions are defined along the longitudinal direction of the MC, including the contributions from the base layer, piezoelectric layer, lower electrode, and upper electrode. Here, the superscripts p, b, e_u, and e_L denote the piezoelectric layer, base layer, upper electrode, and lower electrode, respectively.

Considering Eqs. (14) and (15), the Lagrangian of the system can be written as:

$$\delta(T - U + W_{nc}) = \frac{1}{2}\int_0^{L}\delta[m_0(x)\dot{v}^2 - K(x)v''^2 - C_P P_t(t)v'' + C\dot{v}]dx \tag{16}$$

Because of the discontinuous multilayer configuration and the variation in cross-sectional geometry, the bending stiffness of the MC is spatially non-uniform. Accordingly, the equivalent bending stiffness $K(x)$ is defined separately for the different structural regions.

For the three regions of the MC, namely the multilayer GPLRC–piezoelectric region, the GPLRC-only region, and the narrowed tip region, the corresponding bending stiffness expressions are given by

$$K(x) = K_1(H_0 - H_{L_1}) + K_2(H_{L_1} - H_{L_2}) + K_3(H_{L_2} - H_L) \tag{17}$$

where

$$K_1 = \sum_{k=1}^{n_L+3} E_k b_k h_k\left\{\frac{h_k^2}{12} + \left[y_n - \left(\sum_{j=1}^{n_L+3} h_j - \frac{h_k}{2}\right)\right]^2\right\} \tag{18}$$

$$K_2 = \sum_{k=1}^{n_L} E_k b_k h_k\left\{\frac{h_k^2}{12} + \left[y_{GPL} - \left(\sum_{j=1}^{n_L} h_j - \frac{h_k}{2}\right)\right]^2\right\} \tag{19}$$

$$K_3 = w_t\sum_{k=1}^{n_L} E_k\, b_k h_k\left\{\frac{h_k^2}{12} + \left[y_{GPL} - \left(\sum_{j=1}^{n_L} h_j - \frac{h_k}{2}\right)\right]^2\right\} \tag{20}$$

The neutral-axis position of the multilayer cross-section (y_n) and the location of the GPLRC layer (y_{GPL}) are determined from

$$y_n = \sum_{k=1}^{n_L+3} E_k b_k h_k\left(\sum_{j=1}^{k} h_j - \frac{h_k}{2}\right) \Big/ \sum_{k=1}^{n_L+3} E_k b_k h_k \tag{21}$$

$$y_{GPL} = \sum_{k=1}^{n_L} E_i b_i h_i\left(\sum_{j=1}^{k} h_j - \frac{h_k}{2}\right) \Big/ \sum_{k=1}^{n_L} E_k b_k h_k \tag{22}$$

These expressions account for the redistribution of stiffness and mass resulting from the multilayer GPLRC configuration, the piezoelectric layer, and the geometrical discontinuity near the free end.

The electromechanical coupling coefficient of the piezoelectric layer is defined as

$$C_P = \frac{1}{2} E_P d_{31} b_P \left(\sum_{k=1}^{n_L+3} h_k - \frac{h_p}{2} - y_n \right) P(t) \left(H_0 - H_{L_1} \right) \tag{23}$$

where b_P and h_P denote the width and thickness of the piezoelectric layer, respectively.

Based on Eq. (16), the governing differential equation of motion for the piezoelectric GPLRC MC can be obtained as:

$$m_0(x)v''(x,t) + \left[K(x)v''(x,t)\right]'' + C\dot{v} + C_P''(x)P(t) = 0 \tag{24}$$

The MC is clamped at $x = 0$ and free at $x = L$. The attached nanoparticle is assumed to be concentrated at the free end of the MC. Accordingly, the corresponding boundary conditions are expressed as

$$v(0,t) = 0$$
$$v'(0,t) = 0 \tag{25}$$

$$v''(L,t) = 0$$
$$K(L)v'''(L,t) = m_a v''(L,t) \tag{26}$$

These boundary conditions, together with the piecewise bending stiffness and mass distributions, establish the complete dynamic model of the piezoelectric GPLRC MC and provide the basis for the subsequent modal analysis and evaluation of its mass-sensing characteristics.

In an air environment, the damping coefficient C of the MC is primarily associated with its interaction with the surrounding air and can be estimated from modal analysis using the experimentally measured quality factor. In a liquid environment, however, the dynamic response becomes more complex because the surrounding fluid introduces additional hydrodynamic loading. In particular, the fluid-induced force associated with the compression and displacement of the liquid near the MC surface contributes to both the effective inertia and damping of the structure. These effects are especially relevant for biosensing applications in which the MC operates while immersed in liquid and may vibrate in close proximity to the container bottom, where confined-fluid effects can further resist the cantilever motion.

Two general approaches have been adopted to model MC vibration in liquid environments. The first is the inviscid-fluid formulation, in which the viscosity of the surrounding liquid is neglected. This approximation is generally appropriate when viscous effects are sufficiently weak. The second approach explicitly incorporates fluid viscosity into the vibration model. Among the available viscous formulations, the string-of-spheres model provides a convenient representation of fluid–structure interaction by accounting for both viscous and hydrodynamic effects [41]. In this model, the MC is represented by a string of interconnected spheres, and the fluid-induced forces acting on the spheres are transferred to the cantilever. The resulting hydrodynamic force acting on the MC is therefore expressed as:

$$F_h(x,t) = -\left(0.6\rho_{liq} L_i^{0.5} w^{1.5}\right)\ddot{v} - \left(3\pi\eta + \frac{3}{4}\pi w^2 \sqrt{2\eta\rho_{liq}\Omega}\right)\dot{v} \tag{27}$$

where ρ_{liq} and η denote the density and dynamic viscosity of the surrounding liquid, respectively. In the present study, Ω is taken as the resonance frequency of the MC, consistent with biosensor operation under resonant excitation.

As indicated by Eq. (27), the fluid-induced damping and compression forces are related to the local velocity and acceleration of the MC, respectively. Their effects can therefore be incorporated into the governing differential equation in Eq. (1) by modifying the corresponding damping and inertia terms, c_0 and m_0. Accordingly, the effective damping and mass coefficients are written as:

$$m(x) = m_0(x) + \left(0.6\rho_{liq}L_i^{0.5}w^{1.5}\right) \tag{28}$$

$$c = c_0 + \left(3\pi\eta + \frac{3}{4}\pi w^2\sqrt{2\eta\rho_{liq}\Omega}\right) \tag{29}$$

4. Modal Analysis of the Piezoelectric GPLRC MC

To investigate the resonant behavior and mass-sensing characteristics of the proposed microcantilever (MC), a modal analysis is performed based on the governing equation of motion developed in Section 3. Since the sensing mechanism relies on changes in the resonance characteristics following nanoparticle adsorption, the natural frequencies and corresponding mode shapes of the MC are first determined. The displacement field is expressed in terms of the vibration modes and their associated generalized coordinates as

$$v(x,t) = \sum_{n=1}^{\infty} \varphi_n(x)q_n(t) \tag{30}$$

where represents the nth mode shape of the MC and $q_n(t)$ denotes the corresponding generalized modal coordinate.

Owing to the non-uniform configuration of the proposed MC, which results from the integration of the piezoelectric layer and the narrowed tip region, the structure is divided into three uniform beam segments. The spatial variation of the bending stiffness and mass distribution across these segments must therefore be incorporated into the modal formulation. Accordingly, the mode shape is defined piecewise over the three structural regions as

$$\varphi_n(x) = \begin{cases} A_{n1}\,Sin\,\beta_{n1}\,x + B_{n1}\,Cos\,\beta_{n1}\,x + C_{n1}\,Sinh\,\beta_{n1}\,x + D_{n1}\,Cosh\,\beta_{n1}\,x & 0 < x < L_1 \\ A_{n2}\,Sin\,\beta_{n2}\,x + B_{n2}\,Cos\,\beta_{n2}\,x + C_{n2}\,Sinh\,\beta_{n2}\,x + D_{n2}\,Cosh\,\beta_{n2}\,x & L_1 < x < L_2 \\ A_{n3}\,Sin\,\beta_{n3}\,x + B_{n3}\,Cos\,\beta_{n3}\,x + C_{n3}\,Sinh\,\beta_{n3}\,x + D_{n3}\,Cosh\,\beta_{n3}\,x & L_2 < x < L \end{cases} \tag{31}$$

where A_{ni}, B_{ni}, C_{ni}, and D_{ni} are the unknown coefficients associated with the ith beam segment, and the corresponding wavenumber parameter is defined as $\beta_{ni} = \sqrt[4]{\rho A\omega_n^2/K}$.

The unknown coefficients in Eq. (31) are determined by imposing the clamped boundary condition at the fixed end, the free-end boundary conditions, and the continuity conditions at the interfaces between adjacent segments. In addition, the mode shapes are normalized according to the adopted mass-normalization condition. Applying these conditions leads to a homogeneous system of algebraic equations, which can be expressed in matrix form as

$$J(\beta).X = 0 \tag{32}$$

where J denotes the characteristic matrix and X represents the vector of unknown modal coefficients. The characteristic matrix is constructed from the boundary and continuity conditions and can be written as

$$J = \begin{bmatrix} 0 & 1 & 0 & 1 & 0 & 0 \\ 1 & 0 & 1 & 0 & 0 & 0 \\ \sin\beta L_1 & \cos\beta L_1 & \sinh\beta L_1 & \cosh\beta L_1 & -\sin\lambda_2\beta L_1 & -\cos\lambda_2\beta L_1 \\ \cos\beta L_1 & \sin\beta L_1 & \cosh\beta L_1 & \sinh\beta L_1 & -\lambda_2\cos\lambda_2\beta L_1 & -\lambda_2\sin\lambda_2\beta L_1 \\ -\eta_1\sin\beta L_1 & \eta_1\cos\beta L_1 & \eta_1\sinh\beta L_1 & \eta_1\cosh\beta L_1 & \lambda_2^2\sin\lambda_2\beta L_1 & -\lambda_2^2\cos\lambda_2\beta L_1 \\ -\eta_1\cos\beta L_1 & -\eta_1\sin\beta L_1 & \eta_1\cosh\beta L_1 & \eta_1\sinh\beta L_1 & \lambda_2^3\cos\gamma_2\beta L_1 & -\lambda_2^3\sin\lambda_2\beta L_1 \\ 0 & 0 & 0 & 0 & \sin\lambda_2\beta L_2 & \cos\lambda_2\beta L_2 \\ 0 & 0 & 0 & 0 & \lambda\cos\lambda_2\beta L_2 & -\lambda_2\sin\lambda_2\beta L_2 \\ 0 & 0 & 0 & 0 & -\eta_2\lambda_2^2\sin\lambda_2\beta L_2 & -\eta_2\lambda_2^2\cos\lambda_2\beta L_2 \\ 0 & 0 & 0 & 0 & -\eta_2\lambda_2^3\cos\lambda_2\beta L_2 & \eta_2\lambda_2^3\sin\lambda_2\beta L_2 \\ 0 & 0 & 0 & 0 & 0 & 0 \\ 0 & 0 & 0 & 0 & 0 & 0 \end{bmatrix}$$

$$\begin{bmatrix} 0 & 0 & 0 & 0 & 0 & 0 \\ 0 & 0 & 0 & 0 & 0 & 0 \\ -\sinh\lambda_2\beta L_1 & -\cosh\lambda_2\beta L_1 & 0 & 0 & 0 & 0 \\ -\lambda_2\sinh\lambda_2\beta L_1 & -\lambda_2\cosh\lambda_2\beta L_1 & 0 & 0 & 0 & 0 \\ -\lambda_2^2\cosh\lambda_2\beta L_1 & -\lambda_2^2\sinh\lambda_2\beta L_1 & 0 & 0 & 0 & 0 \\ -\lambda_2^3\cosh\lambda_2\beta L_1 & -\lambda_2^3\cosh\lambda_2\beta L_1 & 0 & 0 & 0 & 0 \\ \sinh\lambda_2\beta L_2 & \cosh\lambda_2\beta L_2 & -\sin\lambda_3\beta L_2 & -\cos\lambda_3\beta L_2 & -\sinh\lambda_3\beta L_2 & -\cosh\lambda_3\beta L_2 \\ \lambda_2\cosh\lambda_2\beta L_1 & \lambda_2\sinh\lambda_2\beta L_1 & -\lambda_3\cos\lambda_3\beta L_2 & \lambda_3\sin\lambda_3\beta L_2 & -\lambda_3\cosh\lambda_3\beta L_2 & -\lambda_3\sinh\lambda_3\beta L_2 \\ \eta_2\lambda_2^2\sinh\lambda_2\beta L_1 & \eta_2\lambda_2^2\cosh\lambda_2\beta L_1 & \lambda_3^2\sin\lambda_3\beta L_2 & \lambda_3^2\cos\lambda_3\beta L_2 & -\lambda_3^2\sinh\lambda_3\beta L_2 & -\lambda_3^2\cosh\lambda_3\beta L_2 \\ \eta_2\lambda_2^3\cosh\lambda_2\beta L_1 & \eta_2\lambda_2^3\sinh\lambda_2\beta L_1 & \lambda_3^3\cos\lambda_3\beta L_2 & -\lambda_3^3\sin\lambda_3\beta L_2 & -\lambda_3^3\cosh\lambda_3\beta L_2 & -\lambda_3^3\sinh\lambda_3\beta L_2 \\ 0 & 0 & -\sin\lambda_3\beta L & -\cos\lambda_3\beta L & \sinh\lambda_3\beta L & \cosh\lambda_3\beta L \\ 0 & 0 & -\cos\lambda_3\beta L + M_1 & \sin\lambda_3\beta L + M_2 & \cosh\lambda_3\beta L + M_3 & \sinh\lambda_3\beta L + M_4 \end{bmatrix} \quad (33)$$

where

$$\eta_m = \frac{K_n}{K_{n+1}};\ \lambda_m = \left(\frac{m_n K_1}{m_1 K_n}\right)^{1/4} \quad (34)$$

$$M_1 = \frac{m_a}{m(L)}\beta\alpha_3\sin\alpha_3\beta L;\quad M_2 = \frac{m_a}{m(L)}\beta\alpha_3\cos\alpha_3\beta L;$$
$$M_3 = \frac{m_a}{m(L)}\beta\alpha_3\sinh\alpha_3\beta L;\quad M_4 = \frac{m_a}{m(L)}\beta\alpha_3\cosh\alpha_3\beta L \quad (35)$$

Non-trivial solutions of the homogeneous system require the determinant of the characteristic matrix to vanish. Therefore, the natural frequencies of the MC are obtained from the characteristic equation det(J) = 0.

Solving this equation provides the natural frequencies ω_n and the corresponding mode-shape coefficients for the first three flexural vibration modes. These modal properties are subsequently used to transform the governing partial differential equation into a set of decoupled modal equations.

By substituting the modal expansion given by Eq. (30) into the governing equation of motion and applying the orthogonality of the mode shapes, the spatial dependence is eliminated. Multiplication of the resulting equation by the corresponding mode shape followed by integration over the MC length yields the following ordinary differential equation for the nth modal coordinate:

$$\ddot{q}_n + \omega_n^2 q_n + \mu_n\dot{q}_n = \chi_n P(t) \quad (36)$$

where μ_n is the modal damping ratio, and

$$\omega_n^2 = \int_0^L \varphi_n(x)\left[K(x)\varphi_n''(x)\right]'' dx \quad (37)$$

$$\Gamma_n = -\int_0^L \varphi_n(x)C_P''(x)dx \quad (38)$$

The modal formulation accounts for the effects of the non-uniform bending stiffness, distributed mass, piezoelectric electromechanical coupling, and the concentrated mass associated with the adsorbed

nanoparticle. Consequently, the resulting modal equation provides a direct representation of the dynamic response of the proposed resonant mass sensor in terms of its individual vibration modes.

The piezoelectric layer is excited by a harmonic voltage applied across the electrodes. Accordingly, the electrical excitation is assumed to have the form $P(t) = P_0 \cos(\Omega t)$, where P_0 is the excitation amplitude and Ω is the excitation frequency. Under steady-state harmonic excitation, the generalized modal coordinate is expressed as $q_n(t) = A_n \cos(\Omega t)$, where A_n denotes the steady-state amplitude of the nth modal response.

Substitution of the harmonic excitation and response into Eq. (36), followed by separation of the harmonic terms, gives the steady-state modal amplitude as

$$A_n = \frac{\Gamma_n P_0}{\sqrt{[(\omega_n^2 - \Omega^2)^2 + (\mu_n \omega_n \Omega)^2]}} \tag{39}$$

The resulting expression establishes the relationship between the excitation frequency, natural frequency, modal damping, and electromechanical coupling of the piezoelectric MC. In particular, the modal amplitude becomes significant when the excitation frequency approaches the corresponding natural frequency.

Since the proposed device operates as a resonant mass sensor, the excitation frequency is selected close to the natural frequency of the mode of interest, i.e., $\Omega \approx \omega_n$. Under this resonant condition, adsorption of a nanoparticle at the free end introduces additional inertial loading and consequently modifies the natural frequency and modal response of the MC. The resulting variation in resonance frequency provides the primary mass-sensing mechanism, while the corresponding changes in vibration amplitude and piezoelectric output can be used as complementary sensing responses.

5. Numerical Simulation

The dynamic behavior and sensing performance of the proposed piezoelectric GPLRC microcantilever (MC) are investigated using the developed theoretical model. The governing equation of motion is formulated based on Hamilton's principle and Euler–Bernoulli beam theory, accounting for the multilayer structure, piezoelectric actuation, and nanoparticle adsorption at the free end.

The MC is actuated by applying an alternating voltage across the electrodes covering the piezoelectric layer, thereby inducing bending vibrations through electromechanical coupling. Its mass-sensing capability is evaluated by examining the changes in resonant characteristics resulting from nanoparticle adsorption at the free end. Accordingly, the effects of the adsorbed mass on the resonant frequency, frequency shift, and electrical output response are systematically investigated.

The geometric dimensions and material properties of the multilayer MC are summarized in Table 1. The electrodes are assumed to fully cover the piezoelectric layer; hence, their lengths and widths are identical to those of the piezoelectric layer. The transverse piezoelectric coefficient of the piezoelectric material is set to d_{31}=11 pC/N.

The functionally graded multilayer GPLRC layer is modeled as a nanocomposite comprising graphene platelets (GPLs) dispersed within an epoxy matrix. The GPLs are characterized by a length of L_{GPL}=2.5 μm, a width of b_{GPL} =1.5 μm, and a thickness of t_{GPL} =1.5 nm. Several GPL distribution patterns are considered to assess their effects on the mechanical behavior, dynamic response, and mass-sensing performance of the proposed MC.

Table 1 Geometrical and material properties of the piezoelectric MC [8]

Geometrical properties			**Material properties**	
h (μm)	W (μm)	L (μm)	E (Gpa)	ρ (Kg/m^3)

Tip	5.0	55	137	GPLRC	Matrix	Epoxy	3	1200
						Polypropylene	0.944	900
Base Layer	5.0	250	350			Polyamide 6	2	1130
					GPL		1010	1062.5
Piezoelectric Layer	5.0	130	330	Piezoelectric			180	2330

To accurately model the functionally graded GPLRC layer as a multilayer structure, an appropriate number of layers must be selected to capture the variation in material composition and effective properties across the thickness. Accordingly, a natural-frequency convergence analysis is conducted for different numbers of layers and GPL distribution patterns. The results demonstrate that a minimum of 12 layers is sufficient to accurately approximate the functionally graded GPLRC MC, as further increasing the number of layers produces negligible changes in the predicted natural frequencies. Therefore, 12 layers are employed in all subsequent simulations, providing a suitable balance between computational efficiency and modeling accuracy across all considered GPLRC configurations.

To validate the proposed analytical model, a dynamic micro-actuated silicon probe (DMASP) microcantilever manufactured by Veeco Instruments was adopted as a reference structure. The experimental first-mode frequency, measured before and after nanoparticle adsorption, was reported in [42]. The corresponding geometrical and material properties were adopted, and the natural frequency was obtained by solving the characteristic Eq. (33) of the developed model.

The predictions are compared with the measurements in Table 2. Before mass deposition, the model gives 53.094 kHz against a measured value of 54.257 kHz (2.189% difference). After adsorption, the corresponding values are 53.044 and 54.218 kHz (2.212%). The nearly identical deviations indicate a small systematic offset, plausibly due to uncertainties in the reported dimensions and material properties and to the idealized clamped boundary, rather than an error in the treatment of the adsorbed mass. The model also reproduces the adsorption-induced frequency decrease, which is 0.050 kHz in the prediction and 0.039 kHz in the experiment, an absolute difference of about 11 Hz.

To verify the model for vibration in liquids with geometric discontinuity, the experimental results of Vázquez et al. [43] for the same DMASP microcantilever in water and in water–glycerol mixtures (10–40%) were also used. Table 3 compares the first-mode resonance frequency and amplitude. The deviations range from 0.3% to 2.3% in frequency and from 2.0% to 5.1% in amplitude, with the largest values in the 40% mixture. The model also follows the experimental trends. From water to the 40% mixture, the measured frequency drops from 16.00 to 14.88 kHz and the predicted one from 16.18 to 15.23 kHz. The measured amplitude falls from 0.84 to 0.59 nm and the predicted one from 0.87 to 0.56 nm. These trends reflect the growing added fluid mass and viscous dissipation.

Overall, the agreement in air, before and after nanoparticle adsorption, and in liquids of different densities and viscosities shows that the proposed model predicts the dynamic behavior of the microcantilever reliably. It is therefore suitable for the analyses presented in the following sections.

Table 2. Predicted and measured natural frequency (kHz) of the DMASP microcantilever before and after nanoparticle adsorption.

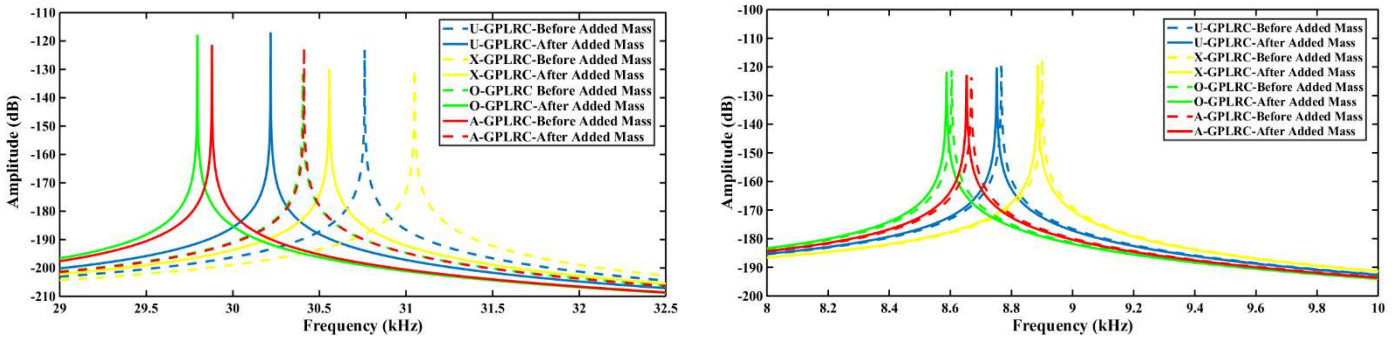
Before mass deposition			**After mass deposition**		
Experimental Results [42]	Analytical Results	Difference (%)	Experimental Results [42]	Analytical Results	Difference (%)
54.257	53.094	2.189	54.218	53.044	2.212

Table 3. Predicted and measured first-mode resonance frequency and amplitude of the DMASP microcantilever in water and water–glycerol mixtures.

	Resonance Frequency (kHz)			Resonance Amplitude (nm)		
	Experimental Results [43]	Analytical Results	Difference (%)	Experimental Results [43]	Analytical Results	Difference (%)
Water	16.00	16.18	1.1	0.84	0.87	3.5
Water-Glycerol 10%	15.89	15.94	0.3	0.76	0.78	2.0
Water-Glycerol 20%	15.64	15.75	0.7	0.72	0.70	2.8
Water-Glycerol 30%	15.31	15.56	1.6	0.66	0.63	4.5
Water-Glycerol 40%	14.88	15.23	2.3	0.59	0.56	5.1

Figure 2 presents the frequency-response characteristics of the piezoelectric microcantilever with a GPLRC substrate before and after adsorption of a 20ng nanoparticle in (a) air and (b) water. As observed, nanoparticle adsorption consistently shifts the resonance peaks toward lower frequencies for all GPLRC configurations in both environments, which is attributed to the increase in the effective modal mass of the microcantilever induced by the adsorbed nanoparticle, while the structural stiffness remains essentially unaffected. The magnitude of this frequency shift varies with the GPLRC arrangement, indicating that the spatial distribution of graphene platelets influences the modal mass and stiffness distribution, and consequently governs the sensitivity of the structure to mass loading. In addition to the resonance-frequency shift, nanoparticle adsorption also alters the resonance amplitude, demonstrating that mass loading simultaneously affects both the frequency and amplitude characteristics of the dynamic response.

A comparison between Fig. 2(a) and Fig. 2(b) further reveals that the resonance-frequency shift induced by the same 20 ng nanoparticle is consistently smaller in water than in air. This reduction is attributed to the additional hydrodynamic mass associated with the surrounding fluid, which increases the effective inertia of the microcantilever and thereby diminishes the relative contribution of the adsorbed nanoparticle to the total modal mass. The aqueous environment also introduces fluid-induced damping, which further modifies the resonance amplitude and contributes to the attenuated dynamic response observed in liquid. Overall, these results demonstrate the pronounced influence of both the GPLRC arrangement and the operating environment on the dynamic response and sensing performance of the proposed mass sensor.



(a) (b)

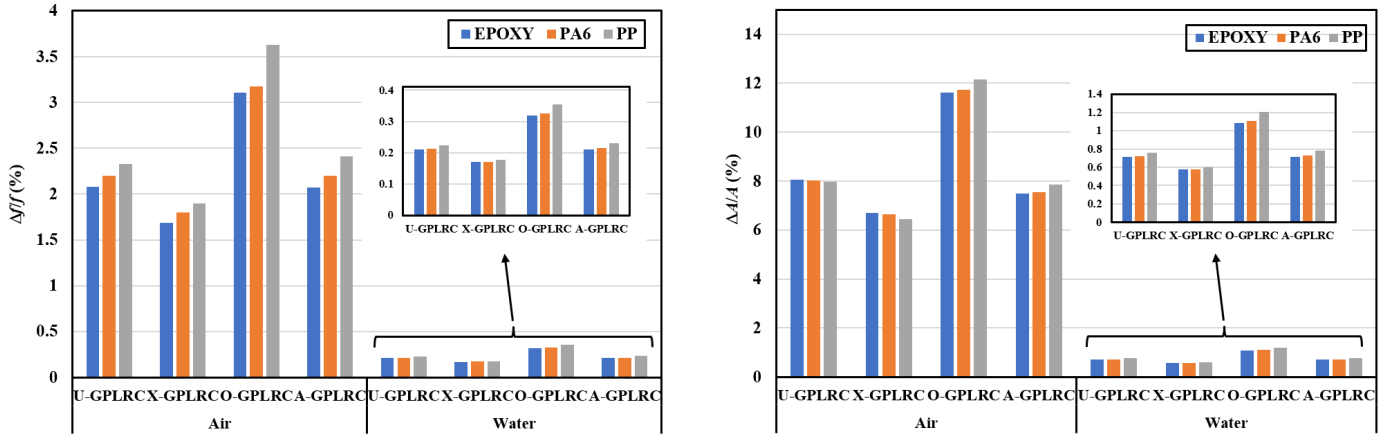
Fig. 2. Frequency-response characteristics of the GPLRC-based piezoelectric microcantilever before and after adsorption of a 20-ng nanoparticle in (a) air and (b) water for different GPLRC configurations.

As observed in Fig. 3(a), the mass-induced frequency shift is consistently lower in the liquid environment than in air, by nearly an order of magnitude (see the inset for the water results), which is attributed to the added mass and viscous damping effects imposed by the surrounding fluid. In both media, the PP matrix yields the largest frequency variation, followed by PA6 and epoxy, although the differences between the matrices are

small, particularly for the X-GPLRC configuration in water. The O-GPLRC configuration provides the highest response among the four arrangements, with Δf/f of about 3.63% in air and 0.35% in water for the PP matrix, whereas X-GPLRC gives the lowest response and U- and A-GPLRC lie in between with similar values. Hence, the effect of the GPL distribution on the frequency shift is stronger than that of the matrix, and the ranking of the distributions (O > U ≈ A > X) is preserved when the medium changes from air to water.

A similar trend is observed for the amplitude response in Fig. 3(b). The O-GPLRC configuration again gives the largest amplitude variation, reaching about 12.15% in air and 1.18% in water for the PP matrix, while X-GPLRC gives the smallest, and the amplitude response in water is again nearly an order of magnitude lower than in air. The influence of the matrix is weaker and less uniform than for the frequency response: for the O- and A-GPLRC configurations, the PP matrix gives the largest amplitude variation in both media, whereas for the U- and X-GPLRC configurations in air the epoxy matrix gives marginally higher values than PP. In water, PP gives the largest amplitude variation for all four configurations, although the differences between the matrices remain small. This indicates that the amplitude is governed mainly by the GPL distribution, with the matrix playing a secondary role.

Overall, these results demonstrate that the GPL distribution has the dominant influence on the mass-induced changes in both frequency and amplitude, with O-GPLRC being the most responsive and X-GPLRC the least responsive arrangement in both air and liquid, while the matrix material plays a secondary but consistent role, with PP providing the largest response in most cases. The PP–O-GPLRC combination therefore gives the most pronounced response in both media, and the relative response in water is about an order of magnitude lower than in air for both sensing metrics. These findings underscore the necessity of considering the operating environment together with the GPL distribution pattern and matrix material in the design and optimization of GPLRC-based resonant mass sensors.

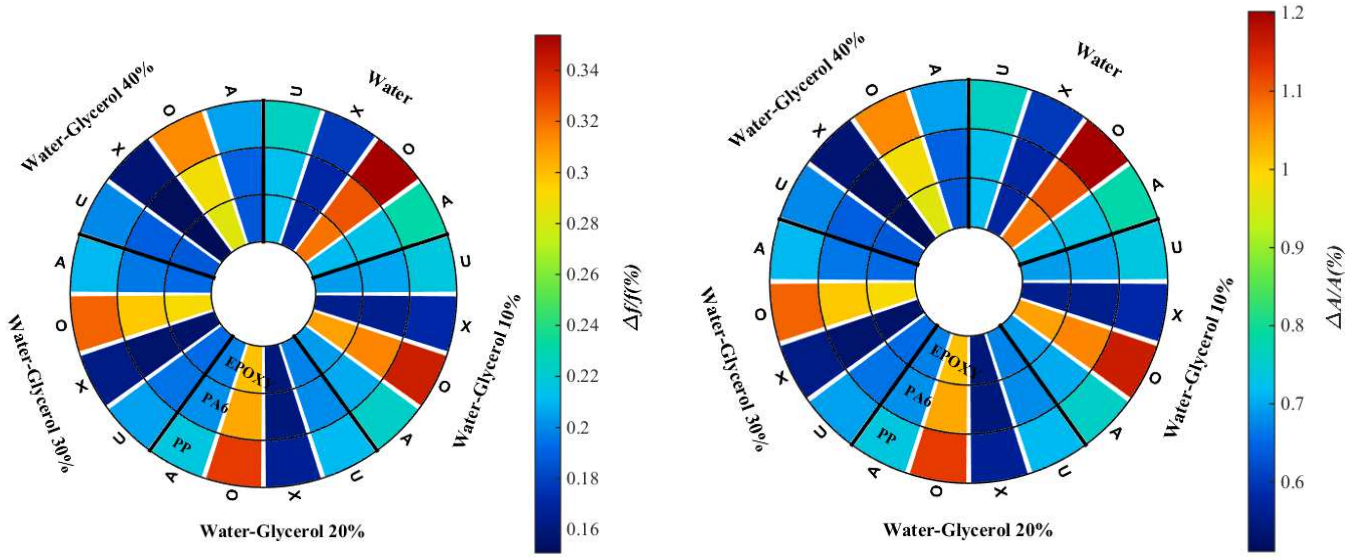


(a) (b)

Figure 3. Relative changes in (a) resonance frequency, Δ*f*/*f*, and (b) vibration amplitude, Δ*A*/*A*, following adsorption of a 20ng nanoparticle mass for different GPLRC matrix materials and layer arrangements in air and liquid environments.

Figure 4 shows the percentage variation in resonance frequency and vibration amplitude following nanoparticle adsorption for the U-, X-, O-, and A-GPLRC configurations, considering different matrix materials and glycerol concentrations. As observed, the largest frequency variation is obtained for the O-GPLRC configuration with the PP matrix, consistent with the trend reported in Fig. 3, and this response decreases progressively with increasing glycerol concentration, from about 0.36% in water to about 0.31% at 40% glycerol, due to the corresponding increase in the density and viscosity of the surrounding medium. The amplitude variation follows the same pattern: it is largest for the O-GPLRC configuration with the PP matrix (about 1.2% in water) and likewise decreases as the glycerol concentration increases, while X-GPLRC gives the smallest values for both metrics. For all configurations and matrix materials, both the frequency- and

amplitude-based responses exhibit a systematic reduction with increasing glycerol concentration, reflecting the combined effect of increased fluid loading and viscous damping, which progressively attenuates the measurable response induced by nanoparticle adsorption. Nevertheless, the dependence of the sensing response on the GPLRC architecture and matrix material remains evident across all liquid environments, as the ordering of the distributions (O > U ≈ A > X) and the small advantage of the PP matrix over PA6 and epoxy are preserved at every glycerol concentration. These results indicate that the GPL distribution pattern is the main factor determining the sensing response in liquid environments, with the matrix material acting as a secondary factor.

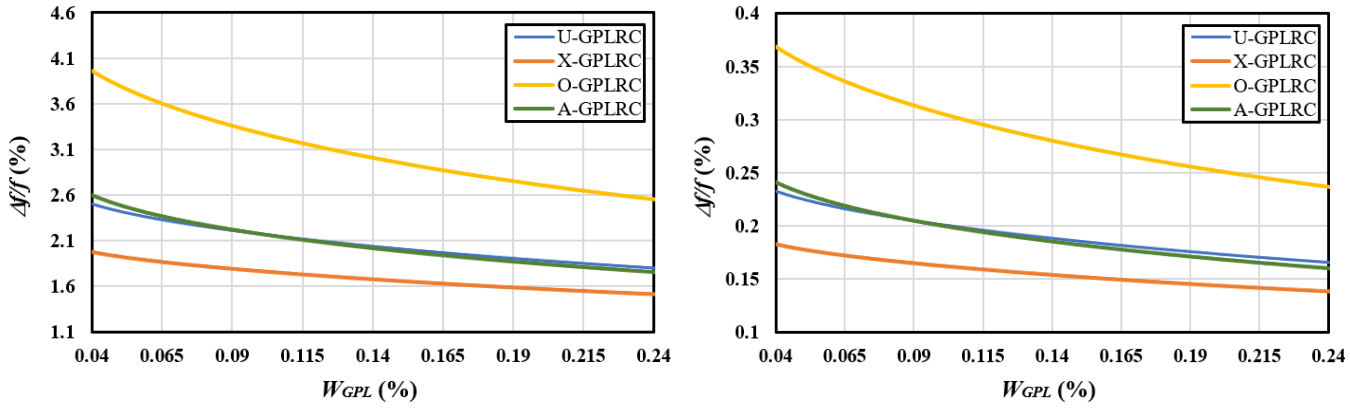


(a) (b)

Figure 4. Percentage variations in (a) resonance frequency, $\Delta f/f$ (%), and (b) resonance amplitude, $\Delta A/A$ (%), following nanoparticle adsorption for different GPLRC layer arrangements and matrix materials in water and water–glycerol mixtures with different glycerol concentrations.

Figure 5 shows the variation of Δf/f (%) with W_{GPL} for the U-, X-, O-, and A-GPLRC configurations in (a) air and (b) water environments, allowing a direct comparison of the sensing response between the two media. As observed, the overall trend with respect to W_{GPL} is the same in Fig. 5(a) and Fig. 5(b) Δf/f decreases monotonically with increasing W_{GPL} for all configurations in both environments, due to the corresponding rise in effective bending stiffness, which reduces the relative frequency shift induced by the adsorbed mass. The ranking of the configurations is also preserved across the two media: O-GPLRC gives the highest response over the entire W_{GPL} range (from about 3.95% to 2.55% in air and from about 0.37% to 0.24% in water), X-GPLRC gives the lowest (from about 1.97% to 1.52% in air and from about 0.18% to 0.14% in water), and the U- and A-GPLRC curves lie in between and intersect at W_{GPL} of about 0.09%, with A-GPLRC slightly higher below this value and slightly lower above it. However, the magnitude of the sensing response in water (Fig. 5b) is substantially lower than in air (Fig. 5a), with Δf/f values reduced by nearly an order of magnitude across the entire W_{GPL} range. This reduction is attributed to the added mass and viscous loading effects imposed by the surrounding fluid, which increase the effective inertia of the vibrating structure and damp its dynamic response, thereby diminishing the measurable frequency shift induced by nanoparticle adsorption. Notably, the relative decrease of Δf/f over the considered W_{GPL} range is similar in the two media (about 35% for O-GPLRC and about 23% for X-GPLRC), which indicates that the fluid mainly scales down the response, while the effect of W_{GPL} on the sensitivity remains essentially unchanged. These results indicate that the surrounding medium governs the absolute sensitivity of GPLRC-based mass sensors, whereas the influence

of W_{GPL} and of the GPL distribution remains qualitatively and proportionally similar across air and liquid environments.

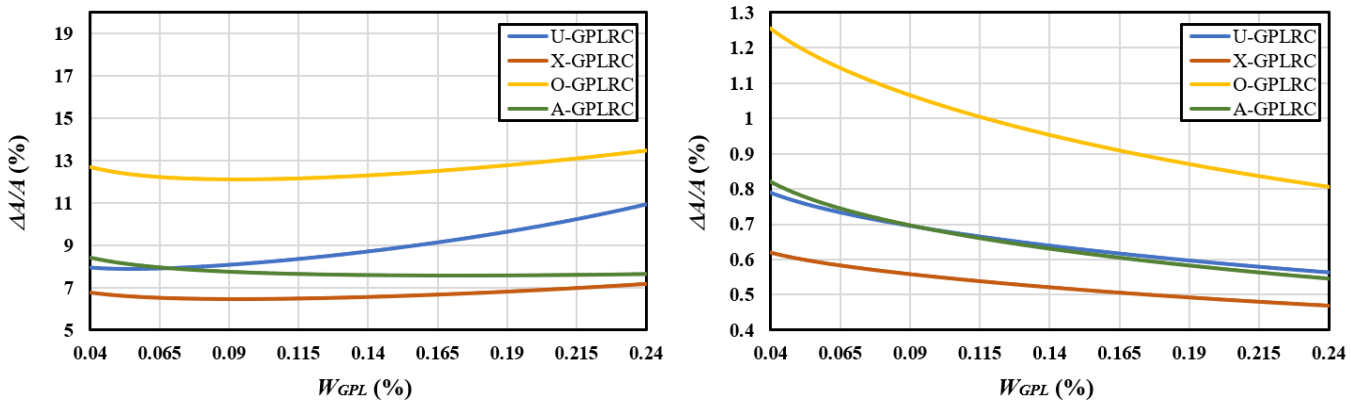


(a) (b)

Figure 5. Percentage variation of resonance frequency ($\Delta f/f$ %) with graphene platelet weight fraction (W_{GPL}) for the U-, X-, O-, and A-GPLRC configurations in (a) air and (b) water environments.

Figure 6 shows the variation of ΔA/A (%) with W_{GPL} for the U-, X-, O-, and A-GPLRC configurations in (a) air and (b) water environments, allowing a direct comparison of the amplitude-based sensing response between the two media. Unlike the frequency-based response discussed in Fig. 5, the amplitude variation in air (Fig. 6a) does not decrease monotonically with W_{GPL} and depends only weakly on it for most configurations. The O-GPLRC configuration provides the highest amplitude variation over the entire W_{GPL} range, decreasing slightly from about 12.7% to about 12.1% at W_{GPL} of about 0.09% and then increasing to about 13.5%. The U-GPLRC configuration increases progressively with W_{GPL}, from about 7.9% to about 11%, and exceeds A-GPLRC for W_{GPL} above about 0.065%. In contrast, A-GPLRC decreases slightly at low W_{GPL} and then remains nearly constant at about 7.6%, while X-GPLRC stays the lowest and varies only modestly, between about 6.5% and 7.2%. This behavior indicates that, unlike the frequency response, the amplitude-based response in air is governed by a more complex interplay between stiffness, mass redistribution, and the resulting mode shape associated with each GPLRC arrangement.

In water (Fig. 6b), however, the trend becomes qualitatively similar to that observed for the frequency response, with ΔA/A decreasing monotonically with increasing W_{GPL} for all configurations. The O-GPLRC configuration consistently provides the highest amplitude variation (from about 1.25% to 0.8%), while X-GPLRC yields the lowest response throughout the considered range (from about 0.62% to 0.47%). The U- and A-GPLRC curves lie in between and intersect at W_{GPL} of about 0.09%, with A-GPLRC slightly higher below this value and slightly lower above it. The amplitude variation in water is also nearly an order of magnitude lower than in air. This behavior is attributed to the dominant influence of fluid loading and viscous damping in the liquid environment, which suppress the amplitude response and overshadow the mass-redistribution effects that govern the dependence on W_{GPL} in air. Overall, these results demonstrate that, although the O-GPLRC configuration gives the largest amplitude response in both media, the dependence of the amplitude-based metric on W_{GPL} is considerably more sensitive to the surrounding environment than that of the frequency-based metric, being weak and non-monotonic in air but monotonically decreasing in water.



(a) (b)

Figure 6. Percentage variation of vibration amplitude (ΔA/A%) with graphene platelet weight fraction (WGPL) for the U-, X-, O-, and A-GPLRC configurations in (a) air and (b) water environments.

To perform the sensitivity analysis, the Saltelli sampling method was employed to efficiently sample the design space of the GPL geometric parameters [38]. This method, which is based on an extension of Sobol' quasi-random sequences, is widely used for variance-based global sensitivity analysis, as it enables the computation of both first-order and total-order Sobol' sensitivity indices with improved convergence and reduced computational cost compared to conventional random sampling techniques [37]. Using this approach, a large number of samples were generated for each GPL geometric parameter (length a_{GPL}, width b_{GPL}, and thickness t_{GPL}), and the corresponding Δf/f (%) response was evaluated for the four GPLRC configurations, allowing the underlying trend to be extracted despite the scatter inherent in the sampled data.

Figure 7 shows the influence of the GPL geometric parameters, namely (a) a_{GPL}, (b) b_{GPL}, and (c) t_{GPL}, on the percentage variation of resonance frequency (Δf/f %) for the U-, X-, O-, and A-GPLRC configurations in air, obtained using the Saltelli-based sensitivity analysis. The O-GPLRC results are plotted with a scaling factor of 0.77 so that all four configurations fit within the same axis range. As observed in Fig. 7(a) and 7(b), increasing both a_{GPL} and b_{GPL} leads to a gradual decrease in Δf/f (%) for all four configurations, indicating that larger in-plane GPL dimensions reduce the mass-sensing response of the structure. The decrease is more pronounced at small dimensions and levels off beyond about 15 μm. Among the four arrangements, the O-GPLRC configuration exhibits the smallest rate of variation (about 2–3% over the considered range), whereas the X-GPLRC configuration shows the most pronounced decrease (about 7% for a_{GPL} and 12% for b_{GPL}, relative to the value at 1 μm), and U- and A-GPLRC lie in between (about 3–4% for a_{GPL} and 7–8% for b_{GPL}). A comparison between Fig. 7(a) and 7(b) further reveals that the response is more sensitive to variations in b_{GPL} than in a_{GPL}, suggesting that the GPL width plays a more significant role than its length in governing the mass-sensing performance.

In contrast, as shown in Fig. 7(c), Δf/f (%) increases progressively with increasing GPL thickness (t_{GPL}) for all four configurations, with the rate of increase gradually decreasing at larger thicknesses. Similar to the trend observed for a_{GPL} and b_{GPL}, the O-GPLRC configuration exhibits the lowest rate of variation with respect to t_{GPL} (about 2–3% over the range of 5–60 nm), while the X-GPLRC configuration shows the highest (about 12%), and U- and A-GPLRC change by about 7%. The ranking of the configurations is the same for all three parameters, with O-GPLRC providing the highest response, X-GPLRC the lowest, and U- and A-GPLRC lying in between with closely comparable values whose scatter bands largely overlap. Overall, these results indicate that the geometric parameters of the graphene platelets, particularly their width and thickness, have a considerable influence on the sensing response, and that the O-GPLRC configuration consistently demonstrates the least sensitivity to variations in GPL geometry, while the X-GPLRC configuration remains the most sensitive across all three parameters.

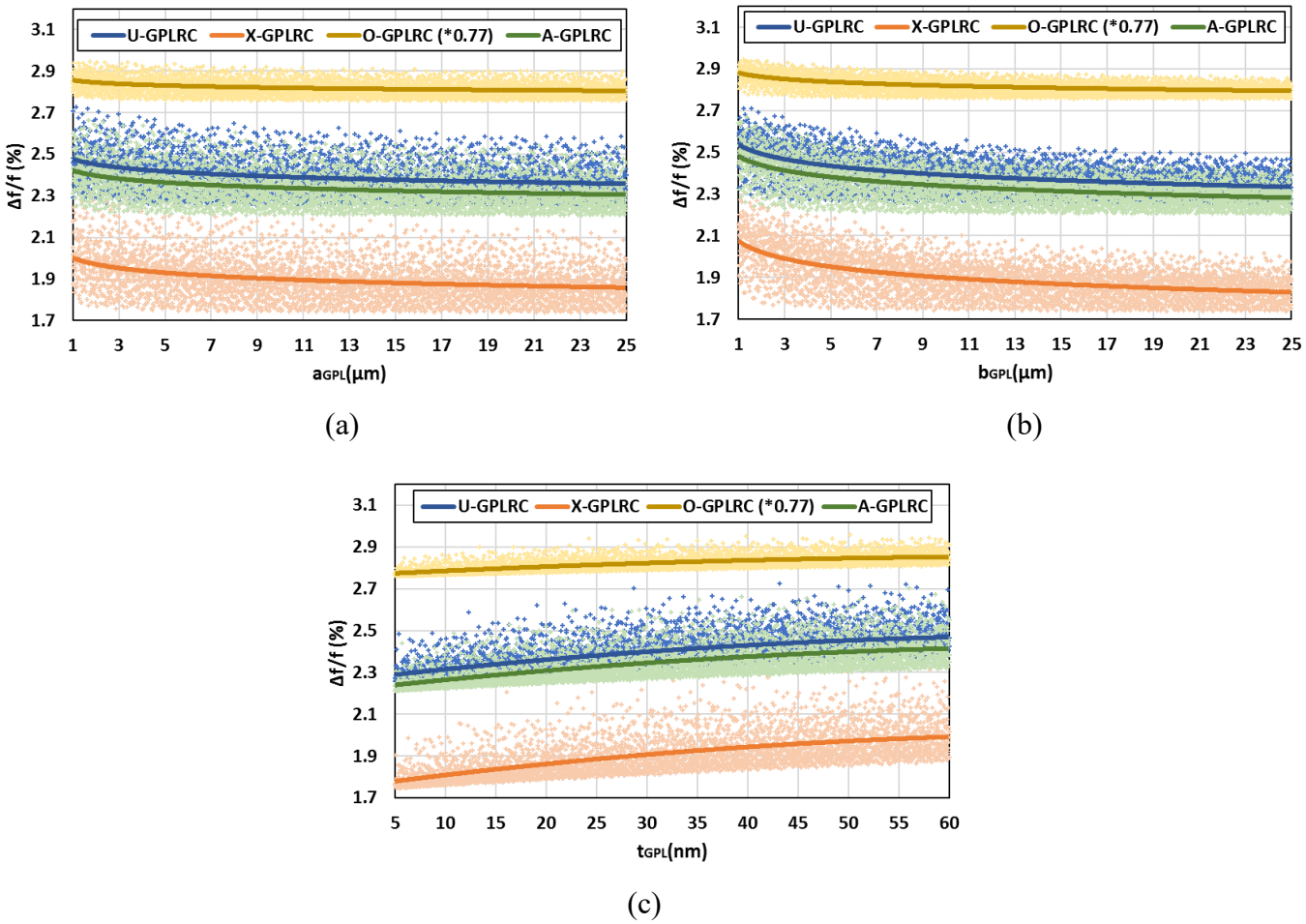


Figure 7. Influence of GPL geometric parameters on the percentage variation of resonance frequency (Δf/f%) for the U-, X-, O-, and A-GPLRC configurations in air: (a) GPL length (a_{GPL}), (b) GPL width (b_{GPL}), and (c) GPL thickness (t_{GPL}).

Figure 8 presents the influence of the GPL geometric parameters, namely (a) a_{GPL}, (b) b_{GPL}, and (c) t_{GPL}, on Δf/f (%) for the four GPLRC configurations in water, obtained using the same Saltelli-based sensitivity analysis as in Fig. 7. Compared with the air results, the overall ranking among the configurations remains unchanged, with O-GPLRC consistently providing the highest Δf/f (%) and X-GPLRC the lowest, while U- and A-GPLRC exhibit intermediate and closely comparable responses. The qualitative trends with respect to the geometric parameters are also preserved: Δf/f decreases with increasing a_{GPL} and b_{GPL} and increases with increasing t_{GPL}, for all four configurations.

However, two notable differences emerge relative to the air environment. First, the magnitude of Δf/f in water is nearly an order of magnitude smaller than in air, consistent with the attenuating effect of fluid loading and viscous damping discussed for Figs. 5 and 6. Second, the sensitivity of the response to the GPL geometric parameters is markedly reduced in water, as reflected by the flatter trend curves in Fig. 8 compared to Fig. 7; this is particularly evident for the O-GPLRC configuration, whose response remains nearly constant across the entire range of a_{GPL}, b_{GPL}, and t_{GPL}. This behavior indicates that the surrounding fluid not only suppresses the overall magnitude of the frequency-based response but also diminishes the relative influence of the GPL geometric parameters on the sensing performance.

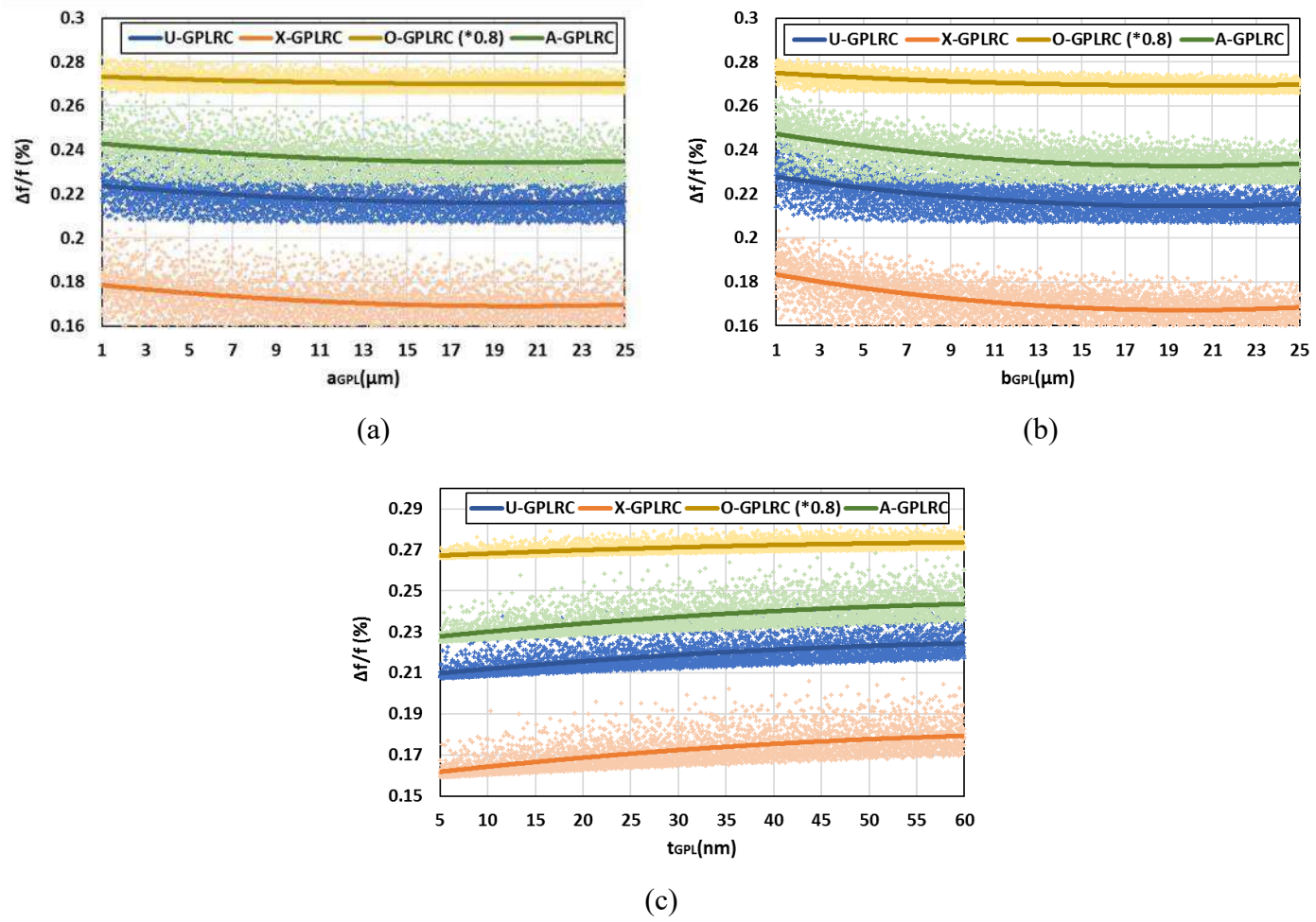


Figure 8. Influence of GPL geometric parameters on the percentage variation of resonance frequency (Δf/f%) for the U-, X-, O-, and A-GPLRC configurations in water: (a) GPL length (a_{GPL}), (b) GPL width (b_{GPL}), and (c) GPL thickness (t_{GPL}).

Figure 9 presents the results of the global Sobol' sensitivity analysis, showing the relative contribution of the GPL geometric parameters (a_{GPL}, b_{GPL}, and t_{GPL}) to the percentage variation of resonance frequency (Δf/f%) for the four GPLRC configurations in (a) air and (b) water environments. As observed, the GPL width (b_{GPL}) exhibits the dominant contribution to the overall sensitivity across all configurations, accounting for approximately 52–54% of the total variance in both air and water, followed by the GPL thickness (t_{GPL}), which contributes around 41–44%. In contrast, the GPL length (a_{GPL}) shows a markedly smaller contribution, remaining below 5% for all four configurations in both environments. This ranking ($b_{GPL} > t_{GPL} \gg a_{GPL}$) is consistent across the U-, X-, O-, and A-GPLRC arrangements, indicating that the relative importance of the GPL geometric parameters is largely governed by the configuration-independent structural mechanics rather than the specific distribution pattern.

A comparison between the air (Fig. 9a) and water (Fig. 9b) results further shows that the relative contributions remain nearly identical between the two environments, with only a marginal decrease in the contribution of a_{GPL} in water (about 4%) compared to air (about 5%), and a correspondingly slight increase in the combined contribution of b_{GPL} and t_{GPL}. This indicates that, despite the significant reduction in the absolute magnitude of Δf/f in water observed in Figs. 7 and 8, the relative importance of the GPL geometric parameters in governing the sensing response remains essentially unaffected by the surrounding fluid medium. Overall, these results confirm that the GPL width is the most influential geometric parameter for the mass-sensing performance of GPLRC-based resonators, regardless of the layer arrangement or operating environment.

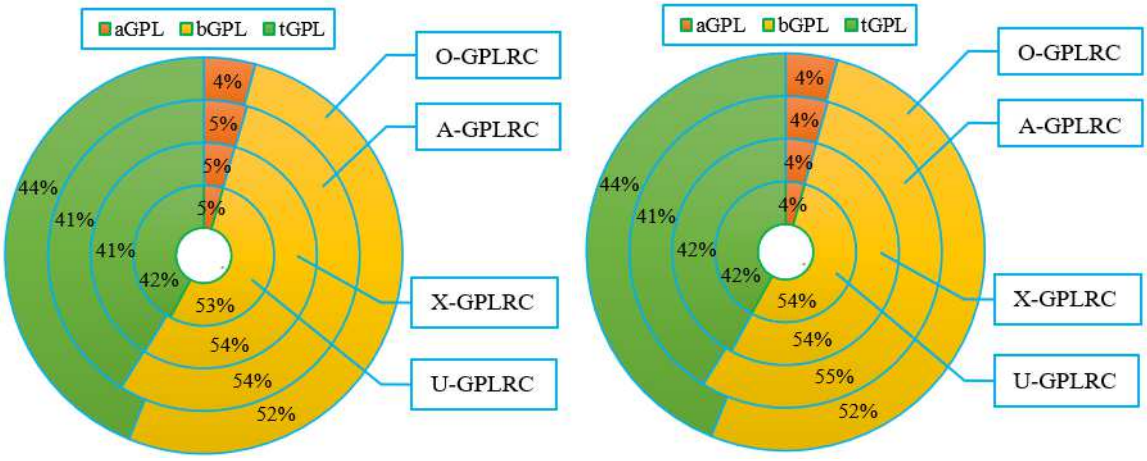


Figure 9. Sobol' sensitivity analysis of GPL geometric parameters (a_{GPL}, b_{GPL}, t_{GPL}) on Δf/f (%) for the four GPLRC configurations in (a) air and (b) water.

6. Conclusions

This study developed an analytical model of a multilayer GPLRC piezoelectric microcantilever with a narrowed tip for resonant mass sensing in air and liquid. The model combines Euler–Bernoulli beam theory, a modified Halpin–Tsai micromechanical formulation, a piecewise modal solution including the adsorbed mass, and a string-of-spheres hydrodynamic model. It was validated against published measurements, with a frequency deviation of about 2.2% in air and within 2.3% in water and water–glycerol mixtures. The main findings are as follows.

1. Nanoparticle adsorption lowered the resonance frequency for all configurations and media. For the same 20 ng mass, the relative frequency shift in water was nearly an order of magnitude smaller than in air, and it decreased further as glycerol concentration increased. This reduction is attributed to added hydrodynamic mass and viscous damping, which dilute the contribution of the adsorbed mass to the total modal inertia.

2. The O-GPLRC distribution gave the largest relative frequency shift in both air and liquid, and the response ranking of the distribution patterns was unchanged between the two media.

3. The most responsive matrix depended on the operating medium. PP gave the largest frequency response in air, whereas PA6 did so in liquid. A matrix that is optimal in air therefore cannot be assumed optimal for liquid-phase sensing.

4. The amplitude response ranked matrices and distributions differently from the frequency response and was more sensitive to the surrounding medium. The choice of readout quantity is thus a design variable in its own right.

5. The relative frequency shift decreased monotonically with GPL weight fraction in both media, because the added stiffness reduces the relative effect of the adsorbed mass. The amplitude response in air did not follow this monotonic trend.

6. The relative frequency shift decreased with increasing platelet length and width and increased with platelet thickness. The O-GPLRC configuration was the least sensitive to these geometric variations, and the X-GPLRC configuration the most. In water, the sensitivity to GPL geometry was markedly reduced.

7. The Sobol' analysis showed that platelet width (52–54% of the output variance) and thickness (41–44%) dominate the frequency response, whereas length contributes less than 5%. This ranking was the same for all four distributions and for both media, so the relative importance of the geometric parameters is governed mainly by the structural mechanics rather than by the distribution pattern or the fluid.

Taken together, the results show that matrix selection, reinforcement architecture, platelet geometry, operating medium, and readout quantity interact and should be chosen jointly when designing GPLRC-based resonant mass sensors. A frequency ranking obtained in air should not be transferred directly to liquid operation.

Funding Declaration

The authors received no financial support for the research, authorship, and/or publication of this article.

References

[1] Mouro, J., et al., *Microcantilever: dynamical response for mass sensing and fluid characterization.* Sensors, 2020. **21**(1): p. 115.
[2] Parkin, J.D. and G. Hähner, *Mass determination and sensitivity based on resonance frequency changes of the higher flexural modes of cantilever sensors.* Review of Scientific Instruments, 2011. **82**(3).
[3] Darban, H., *Size effect in ultrasensitive micro-and nanomechanical mass sensors.* Mechanical Systems and Signal Processing, 2023. **200**: p. 110576.
[4] Wei, Y., et al., *Micro-mass sensor-based vibration response of smart bidirectional functionally graded auxetic microbeams.* Archives of Civil and Mechanical Engineering, 2024. **24**(1): p. 38.
[5] Darban, H., R. Luciano, and M. Basista, *Modeling frequency shifts in small-scale beams with multiple eccentric masses.* Thin-Walled Structures, 2024. **201**: p. 112005.
[6] Adhikari, S., *Inertial mass sensing with low Q-factor vibrating microcantilevers.* Journal of Applied Physics, 2017. **122**(14).
[7] Shin, S., et al., *A multisized piezoelectric microcantilever biosensor array for the quantitative analysis of mass and surface stress.* Applied Physics Letters, 2008. **93**(10).
[8] Faegh, S., N. Jalili, and S. Sridhar, *A self-sensing piezoelectric microcantilever biosensor for detection of ultrasmall adsorbed masses: theory and experiments.* Sensors, 2013. **13**(5): p. 6089–6108.
[9] Daniel, V., O. Auciello, and E. de Obaldia, *Design of a Piezoelectrically Actuated Ultrananocrystalline Diamond (UNCD) Microcantilever Biosensor.* Applied Sciences, 2025. **15**(12): p. 6902.
[10] Nsubuga, L., et al., *Gas adsorption response of piezoelectrically driven microcantilever beam gas sensors: analytical, numerical, and experimental characterizations.* Sensors, 2023. **23**(3): p. 1093.
[11] Sader, J.E., *Frequency response of cantilever beams immersed in viscous fluids with applications to the atomic force microscope.* Journal of applied physics, 1998. **84**(1): p. 64–76.
[12] van Eysden, C.A. and J. Elie Sader, *Frequency response of cantilever beams immersed in viscous fluids.* Resonant MEMS: Fundamentals, Implementation and Application, 2015: p. 29–53.
[13] Voglhuber-Brunnmaier, T. and B. Jakoby, *Electromechanical resonators for sensing fluid density and viscosity—A review.* Measurement Science and Technology, 2022. **33**(1): p. 012001.
[14] Shih, W.Y., et al., *Simultaneous liquid viscosity and density determination with piezoelectric unimorph cantilevers.* Journal of Applied Physics, 2001. **89**(2): p. 1497–1505.
[15] Huang, L., et al., *Piezoelectric-AlN resonators at two-dimensional flexural modes for the density and viscosity decoupled determination of liquids.* Microsystems & nanoengineering, 2022. **8**(1): p. 38.
[16] Alshammri, A., et al., *Quality factor of a microchannel microresonator as a function of viscosity and its vibrational mode: An experimental and computational analysis.* IEEE Sensors Journal, 2022. **23**(1): p. 104–110.
[17] Tiwari, S., A. Dangi, and R. Pratap, *A tip-coupled, two-cantilever, non-resonant microsystem for direct measurement of liquid viscosity.* Microsystems & nanoengineering, 2023. **9**(1): p. 34.

[18] Huang, L., et al., *Piezoelectric stepped-plate resonators vibrating at lateral modes for direct viscosity determination in liquids.* Microsystems & Nanoengineering, 2026. **12**(1): p. 122.
[19] Qu, S. and C. Xia, *An Enhanced Q-Factor Cantilever Resonator in Viscous Liquids Using Strategic Perforation.* Micromachines, 2026. **17**(3): p. 385.
[20] Reif, J., et al., *Enhanced mechanical properties of nanocomposites at low graphene content.* ACS nano, 2009. **3**(12): p. 3884–3890.
[21] Ramos, V.D., et al., *Effect of graphene nanoplatelets (GNPs) incorporation on the mechanical and thermal properties of polyamide 6.* Journal of Thermoplastic Composite Materials, 2026. **39**(5): p. 2195–2229.
[22] Ulutas, E. and M. Tasdemir, *Comparative Analysis of Solid and Foamed PA6 Composite Architectures Reinforced With Graphene Nanoplatelets.* Polymer Engineering & Science, 2026.
[23] Jun, Y., et al., *A study on the effects of graphene nano-platelets (GnPs) sheet sizes from a few to hundred microns on the thermal, mechanical, and electrical properties of polypropylene (PP)/GnPs composites.* Express Polym. Lett, 2018. **12**(10): p. 885–897.
[24] Patra, S.C., et al., *Polypropylene and graphene nanocomposites: effects of selected 2D-nanofiller's plate sizes on fundamental physicochemical properties.* Inventions, 2022. **8**(1): p. 8.
[25] Dananjaya, V. and C. Abeykoon, *Thermo-mechanical and electrical properties of graphene nanoplatelets reinforced recycled polypropylene nanocomposites.* International Journal of Lightweight Materials and Manufacture, 2025. **8**(3): p. 374–384.
[26] Tam, M., et al., *Vibration and buckling characteristics of functionally graded graphene nanoplatelets reinforced composite beams with open edge cracks.* Materials, 2019. **12**(9): p. 1412.
[27] Babaei, M., et al., *Three dimensional free vibration analysis of functionally graded graphene reinforced composite laminated cylindrical panel.* Proceedings of the Institution of Mechanical Engineers, Part L: Journal of Materials: Design and Applications, 2022. **236**(8): p. 1501–1514.
[28] Liu, D., *Free vibration of functionally graded graphene platelets reinforced magnetic nanocomposite beams resting on elastic foundation.* Nanomaterials, 2020. **10**(11): p. 2193.
[29] Lawongkerd, J., et al., *Vibration characteristics of multilayer functionally graded microplates with variable thickness reinforced by graphene platelets resting on the viscoelastic medium under thermal effects.* International Journal of Thermofluids, 2024. **22**: p. 100611.
[30] Roun, S., V.-L. Nguyen, and J. Rungamornrat, *Free vibration and buckling analyses of functionally graded plates with graphene platelets reinforcement.* Journal of Computing and Information Science in Engineering, 2025. **25**(1): p. 011002.
[31] Mao, J., et al., *Vibrations of graphene nanoplatelet reinforced functionally gradient piezoelectric composite microplate based on nonlocal theory.* Composite Structures, 2020. **236**: p. 111813.
[32] Nguyen, V.-L., et al., *Free vibration analysis of smart piezoelectric GPL-reinforced FGM microplates placed on Winkler–Pasternak foundation: V.-L. Nguyen et al.* Acta Mechanica, 2026. **237**(1): p. 153–179.
[33] Nguyen, V.-L., et al., *Electro-thermal vibration of graphene platelets reinforced functionally graded piezoelectric microplates under different boundary conditions.* International Journal of Solids and Structures, 2025. **314**: p. 113273.
[34] Jiang, Y., et al., *Vibration attenuation of FG–GR-laminated composite cantilever rectangular plate integrated with piezoelectric actuator and sensor.* Journal of Vibration Engineering & Technologies, 2024. **12**(4): p. 6885–6906.
[35] Wu, H., et al., *Free vibration analysis of functionally graded graphene nanocomposite beams partially in contact with fluid.* Composite Structures, 2022. **291**: p. 115609.
[36] Tofangsaz, A., et al., *Free vibration analysis of graphene reinforced functionally graded nanocomposite plates in contact with quiescent bounded fluids on both sides.* Applied Ocean Research, 2024. **147**: p. 103989.
[37] Sobol, I.M., *Global sensitivity indices for nonlinear mathematical models and their Monte Carlo estimates.* Mathematics and computers in simulation, 2001. **55**(1-3): p. 271–280.
[38] Saltelli, A., et al., *Variance based sensitivity analysis of model output. Design and estimator for the total sensitivity index.* Computer physics communications, 2010. **181**(2): p. 259–270.
[39] Guan, C., et al., *Global sensitivity analysis of complex moduli of carbon fiber reinforced polymer.* Polymer Composites, 2023. **44**(11): p. 7418–7429.
[40] Yang, J., H. Wu, and S. Kitipornchai, *Buckling and postbuckling of functionally graded multilayer graphene platelet-reinforced composite beams.* Composite Structures, 2017. **161**: p. 111–118.

[41] Rankl, C., et al., *Hydrodynamic damping of a magnetically oscillated cantilever close to a surface.* Ultramicroscopy, 2004. **100**(3-4): p. 301–308.
[42] Salehi-Khojin, A., et al., *Nanomechanical cantilever active probes for ultrasmall mass detection.* Journal of Applied Physics, 2009. **105**(1).
[43] Vazquez, J., et al., *Dynamic response of low aspect ratio piezoelectric microcantilevers actuated in different liquid environments.* Journal of Micromechanics and Microengineering, 2009. **19**(1): p. 015020.